ELSEVIER

CrossMark

An adaptive multiresolution method for ideal magnetohydrodynamics using divergence cleaning with parabolic–hyperbolic correction

Anna Karina Fontes Gomes [a,d], Margarete Oliveira Domingues [b,d,∗],
Kai Schneider [e], Odim Mendes [c,d], Ralf Deiterding [f]

[a] *Pós-Graduação em Computação Aplicada (CAP), Brazil*
[b] *Laboratório Associado de Computação e Matemática Aplicada (LAC), Coordenadoria dos Laboratórios Associados (CTE), INPE, Brazil*
[c] *Divisão de Geofísica Espacial (DGE), Coordenação de Ciências Espaciais (CEA), INPE, Brazil*
[d] *Instituto Nacional de Pesquisas Espaciais (INPE), Av. dos Astronautas 1758, 12227-010 São José dos Campos, São Paulo, Brazil*
[e] *M2P2–CNRS & Centre de Mathématiques et d'Informatique (CMI), Aix-Marseille Université, 38 rue F. Joliot-Curie, 13451 Marseille Cedex 20, France*
[f] *German Aerospace Center (DLR), Institute of Aerodynamics and Flow Technology, Bunsenstr. 10, 37073 Göttingen, Germany*

A R T I C L E   I N F O

A B S T R A C T

We present an adaptive multiresolution method for the numerical simulation of ideal magnetohydrodynamics in two space dimensions. The discretization uses a finite volume scheme based on a Cartesian mesh and an explicit compact Runge–Kutta scheme for time integration. Harten's cell average multiresolution allows to introduce a locally refined spatial mesh while controlling the error. The incompressibility of the magnetic field is controlled by using a Generalized Lagrangian Multiplier (GLM) approach with a mixed hyperbolic–parabolic correction. Different applications to two-dimensional problems illustrate the properties of the method. For each application CPU time and memory savings are reported and numerical aspects of the method are discussed. The accuracy of the adaptive computations is assessed by comparison with reference solutions computed on a regular fine mesh.

1. Introduction

The magnetohydrodynamic (MHD) equations, which consist of the compressible Euler equations of hydrodynamics coupled with the Maxwell equations of electrodynamics, are used for mathematical modeling of numerous phenomena encountered in our daily life. Prominent examples can be found in the physics of the Sun–Earth electrodynamics interaction chain, and in the dynamo action caused by motion of liquid metal inside the mantle of the Earth, which generates its magnetic field. The numerical challenge for solving the ideal MHD equations, a coupled set of nonlinear Partial Differential Equations (PDEs), is the presence of multiple spatial and temporal scales. The complex character of boundary conditions of the magnetic field, in comparison to those for classical hydrodynamics, requires even more sophisticated approaches. In a surrounding vacuum, for example, the magnetic field does not vanish, it only decays. Thus, at the boundary it has to be

∗ Corresponding author at: Instituto Nacional de Pesquisas Espaciais (INPE), Av. dos Astronautas 1758, 12227-010 São José dos Campos, São Paulo, Brazil.
E-mail addresses: annakfg@gmail.com (A.K.F. Gomes), margarete.domingues@inpe.br (M.O. Domingues), margarete.oliveira.domingues@gmail.com (M.O. Domingues), kschneid@cmi.univ-mrs.fr (K. Schneider), odim.mendes@inpe.br (O. Mendes), ralf.deiterding@dlr.de (R. Deiterding).

matched with the field of the fluid region. A second difficulty is to maintain the incompressibility of the magnetic field numerically, which is imposed by Gauss's law. Therefore, in the numerical simulations, special attention has to be paid to the incompressibility constraint, because, as shown in practice, uncontrolled divergence errors can modify the underlying physics. For details we refer the reader to, *e.g.*, [2,4,26,29]. Typically, projection methods based on the Helmholtz decomposition are used. These methods are computationally demanding, especially in three dimensions, because the solution of an elliptic problem requires a Poisson equation solver. An alternative method is divergence cleaning, which is based on Lagrangian multipliers. In the finite element context, Assous et al. [1] introduced this approach for time-dependent Maxwell equations. Several variants can be found in the literature [2,4,25,29].

In the current paper we apply the multiresolution approach to an ideal MHD numerical model called the Generalized Lagrange Multiplier (GLM) with a mixed hyperbolic–parabolic correction proposed by Dedner et al. [6] to deal with the incompressibility condition of the magnetic field. The ideas of the Lagrangian multiplier formulation in this situation were introduced by Munz et al. [24] in the context of Maxwell equations. With the motivation to reduce CPU time and memory requirements, we use an auto-adaptive discretization which is based on the multiresolution representation. The underlying time dependent conservation laws are discretized with finite volume schemes and local mesh refinement is triggered by multiresolution analysis of the cell averages and thresholding of the resulting coefficients. The adaptive refinement of the mesh tracks steep gradients in the solution of the equation and thus allows automatic error control. For reviews on multiresolution techniques for PDEs we refer to [17,18,23,13] and references therein.

Preliminary results for a quasi-one dimensional MHD Riemann problem with exact solution have been presented in [10], which showed the feasibility of using adaptive discretizations and magnetic field divergence cleaning for extended GLM–MHD with local and controlled time stepping methods. In its extended form, source terms similar to those in [25] are introduced. The starting point is the adaptive multiresolution code originally developed by Roussel et al. [27] in which the Maxwell equations governing the magnetic field have been included [16]. In the present work, we have chosen the GLM–MHD approach instead of its extended version, because the divergence errors and the solution obtained for both cases are almost the same for the studied problem. A similar choice is suggested in the conclusion in [6]. The resulting new method has been applied to a two-dimensional Riemann test problem, for which a reference solution on a fine mesh has been computed. The accuracy of the adaptive computations has been assessed and their efficiency in terms of memory compression compared to a finite volume scheme on a regular mesh has been analyzed.

This paper is organized as follows: After a presentation of the governing ideal MHD equations in Section 2, we recall the divergence cleaning technique based on the GLM formulation in Section 3. In Section 4, space and time discretizations are briefly described together with the GLM discretization. In Section 5, numerical results are presented. In the last section, some conclusions are drawn and perspectives for future work are given.

2. Governing equations

The ideal magnetohydrodynamic equations describe the dynamics of a compressible, inviscid and perfectly electrically conducting fluid interacting with a magnetic field, see, *e.g.* [15]. The equations combine the Euler equations with the Maxwell equations. The latter yields an evolution equation for the magnetic field, also called induction equation, and an incompressibility constraint using Gauss' law. The system of MHD equations is given by

$$\frac{\partial \rho}{\partial t} + \nabla \cdot (\rho \, \mathbf{u}) = 0, \qquad \text{(Mass conservation)} \tag{1a}$$

$$\frac{\partial E}{\partial t} + \nabla \cdot \left[\left(E + p + \frac{\mathbf{B} \cdot \mathbf{B}}{2} \right) \mathbf{u} - (\mathbf{u} \cdot \mathbf{B}) \, \mathbf{B} \right] = 0, \qquad \text{(Energy conservation)} \tag{1b}$$

$$\frac{\partial \rho \, \mathbf{u}}{\partial t} + \nabla \cdot \left[\rho \, \mathbf{u}^t \, \mathbf{u} + \left(p + \frac{\mathbf{B} \cdot \mathbf{B}}{2} \right) \mathbf{I} - \mathbf{B}^t \, \mathbf{B} \right] = \mathbf{0}, \quad \text{(Momentum conservation)} \tag{1c}$$

$$\frac{\partial \mathbf{B}}{\partial t} + \nabla \cdot \left(\mathbf{u}^t \, \mathbf{B} - \mathbf{B}^t \, \mathbf{u} \right) = \mathbf{0}, \qquad \text{(Induction equation)} \tag{1d}$$

where ρ represents density, p the pressure, $\mathbf{u} = (u_x, u_y, u_z)$ the velocity field, $\mathbf{B} = (B_x, B_y, B_z)$ the magnetic field, and the upper index t denotes the transposition. The identity tensor of order 2 is denoted by $\mathbf{I}$ (which corresponds to the unit matrix 3×3), and γ is the adiabatic constant ($\gamma > 1$).

The pressure is given by the constitutive law

$$p = (\gamma - 1) \left(E - \rho \frac{\mathbf{u} \cdot \mathbf{u}}{2} - \frac{\mathbf{B} \cdot \mathbf{B}}{2} \right).$$

The above system is completed by suitable initial and boundary conditions. In this paper this system is considered in its two-dimensional form, *i.e.*, the quantities depend on two variables only (x and y).

In this classical MHD model, the magnetic field has to satisfy the divergence constraint

$$\nabla \cdot \mathbf{B} = 0, \tag{2}$$

which implies the non-existence of magnetic monopoles. By rewriting the induction equation, we have $\dfrac{\partial \mathbf{B}}{\partial t} + \nabla \times (\mathbf{B} \times \mathbf{u}) = \mathbf{0}$.

Therefore, the application of the divergence operator yields $\dfrac{\partial}{\partial t}(\nabla \cdot \mathbf{B}) = 0$, as $\nabla \cdot (\nabla \times) \equiv 0$. This formulation shows that if the initial condition of the magnetic field is divergence-free, the system will remain divergence-free along its evolution. However, numerically the incompressibility of the magnetic field is not necessarily preserved, and thus, non-physical results could be obtained or the computations may even become unstable [4]. Since the 1980's typical numerical MHD methodologies consider the enforcement of the divergence-free constraint. There are many techniques to perform the divergence cleaning in numerical MHD models [30]. In the context of this study, we have in mind the application of a multiresolution method based on a finite volume discretization with explicit time integration. Thus, the technique developed in Dedner et al. [6], called GLM–MHD with the mixed parabolic–hyperbolic correction, is well suited. Details are given in the next section.

3. Generalized Lagrangian multipliers for divergence cleaning

Dedner et al. [6] proposed the GLM formulation with the hyperbolic–parabolic correction. Its implementation into a pre-existing MHD model is straightforward. An additional scalar field ψ is introduced, which couples the divergence constraint equation (Eq. (2)) to Faraday's law, modifying the induction equation (Eq. (1d)). Moreover, some source terms are added similarly to what was proposed in [25]. The model contains one parameter related to the hyperbolic correction, namely c_h, responsible for the propagation of the divergence errors, and another one related to the parabolic correction c_p, responsible for the damping of the monopoles. The remaining terms in the equations remain unchanged. The conservative characteristics of this system are thus not lost in the GLM approach.

The resulting GLM–MHD equations written in two-dimensional form read

$$\frac{\partial \rho}{\partial t} + \frac{\partial \rho u_x}{\partial x} + \frac{\partial \rho u_y}{\partial y} = 0, \tag{3a}$$

$$\frac{\partial E}{\partial t} + \frac{\partial}{\partial x}\left[\left(E + p + \frac{\mathbf{B} \cdot \mathbf{B}}{2}\right)u_x - (\mathbf{u} \cdot \mathbf{B})B_x\right] + \frac{\partial}{\partial y}\left[\left(E + p + \frac{\mathbf{B} \cdot \mathbf{B}}{2}\right)u_y - (\mathbf{u} \cdot \mathbf{B})B_y\right] = 0, \tag{3b}$$

$$\frac{\partial(\rho u_x)}{\partial t} + \frac{\partial}{\partial x}\left[\rho u_x^2 + \left(p + \frac{\mathbf{B} \cdot \mathbf{B}}{2}\right) - B_x^2\right] + \frac{\partial}{\partial y}\left(\rho u_x u_y - B_x B_y\right) = 0, \tag{3c}$$

$$\frac{\partial(\rho u_y)}{\partial t} + \frac{\partial}{\partial x}\left(\rho u_x u_y - B_x B_y\right) + \frac{\partial}{\partial y}\left[\rho u_y^2 + \left(p + \frac{\mathbf{B} \cdot \mathbf{B}}{2}\right) - B_y^2\right] = 0, \tag{3d}$$

$$\frac{\partial(\rho u_z)}{\partial t} + \frac{\partial}{\partial x}\left(\rho u_z u_x - B_z B_x\right) + \frac{\partial}{\partial y}\left(\rho u_z u_y - B_z B_y\right) = 0, \tag{3e}$$

$$\frac{\partial B_x}{\partial t} + \frac{\partial \psi}{\partial x} + \frac{\partial}{\partial y}\left(u_y B_x - B_y u_x\right) = 0, \tag{3f}$$

$$\frac{\partial B_y}{\partial t} + \frac{\partial}{\partial x}\left(u_x B_y - B_x u_y\right) + \frac{\partial \psi}{\partial y} = 0, \tag{3g}$$

$$\frac{\partial B_z}{\partial t} + \frac{\partial}{\partial x}\left(u_x B_z - B_z u_x\right) + \frac{\partial}{\partial y}\left(u_y B_z - B_y u_z\right) = 0, \tag{3h}$$

$$\frac{\partial \psi}{\partial t} + c_h^2\left(\frac{\partial B_x}{\partial x} + \frac{\partial B_y}{\partial y}\right) = -\frac{c_h^2}{c_p^2}\psi, \tag{3i}$$

where $\mathbf{B} \cdot \mathbf{B} = B_x^2 + B_y^2 + B_z^2$, $\mathbf{u} \cdot \mathbf{B} = u_x B_x + u_y B_y + u_z B_z$, c_p and c_h are the parabolic–hyperbolic parameters, with $c_h > 0$. In [6], c_h is defined as

$$c_h = c_h(t) := c_{CFL}\frac{\min(\Delta x, \Delta y)}{\Delta t}, \tag{4}$$

where $c_{CFL} \in (0, 1)$, Δx and Δy are the space steps in the x- and y-direction, respectively, Δt is the time step. If the parameter c_h is defined, as for instance in Eq. (4), then c_p is a free parameter in Eq. (3i). We follow a choice proposed in [6] to avoid that c_p is strongly dependent on the mesh size and the scheme used. Their numerical experiments showed that choosing $c_p^2/c_h = 0.18$ mirrors properly the ratio between hyperbolic and parabolic effects. With this choice in the one-dimensional case the damping of divergence errors occurs on the time scale $c_p\sqrt{t}$ and the transport of the divergence errors to the boundary takes place on the time scale $c_h t$ (as discussed in [6], Appendix A.16 and A.19). However, other possible choices of these parameters can be found in [31,7] and for the CTU-GLM approach in [21].

Considering the vector of conservative quantities $\mathbf{Q} = (\rho, E, \rho\mathbf{u}, \mathbf{B}, \psi)$, the GLM–MHD system could be written compactly as a conservation law with source terms,

$$\frac{\partial \mathbf{Q}}{\partial t} + \nabla \cdot \mathbf{F}(\mathbf{Q}) = \mathbf{S}(\mathbf{Q}),$$

where $\mathbf{F}(\mathbf{Q})$ is the physical flux and $\mathbf{S}(\mathbf{Q})$ contains all source terms.

4. Adaptive space and time discretization

A finite volume discretization of the GLM–MHD system is applied, which results in a system of ordinary differential equations. Approximate solutions at a sequence of time instants t^n are obtained by using an explicit ordinary differential equation solver. Here, an explicit Runge–Kutta scheme of second order is used.

In the GLM–MHD Finite Volume (FV) reference scheme, we consider the initial value of the variable ψ as zero. The parameter c_h has a strong influence on the correction. In each time step, we compute the parameter c_h, then the GLM–MHD system is solved. First, a dimensional splitting is performed in x-direction, where the fluxes of the interface are treated and the solution is updated. This procedure follows the steps:

1. The component of the magnetic field B_x in the x-direction flux (Eq. (3f)), and the divergence constraint equation (Eq. (3i)), are decoupled from the other variables. These two equations form the system

$$\frac{\partial B_x}{\partial t} + \frac{\partial \psi}{\partial x} = 0,\tag{5}$$

$$\frac{\partial \psi}{\partial t} + c_h^2 \frac{\partial B_x}{\partial x} = -\frac{c_h^2}{c_p^2}\psi,\tag{6}$$

such that the local Riemann problem can be solved analytically, where the numerical flux at the interface is $(\psi_m, c_h^2 B_{x,m})$ for B_x and ψ. Similarly as what is described in [6], we have

$$\begin{pmatrix} B_{x,m} \\ \psi_m \end{pmatrix} = \begin{pmatrix} B_{x,L} \\ \psi_L \end{pmatrix} + \begin{pmatrix} \frac{1}{2}(B_{x,R} - B_{x,L}) - \frac{1}{2c_h}(\psi_R - \psi_L) \\ \frac{1}{2}(\psi_R - \psi_L) - \frac{c_h}{2}(B_{x,R} - B_{x,L}) \end{pmatrix},\tag{7}$$

where the sub-indices L and R are related to the left or right-hand state.

2. The numerical flux is evaluated in two steps. First we compute the numerical flux not considering the B_x and ψ equations as described above. Then we add the numerical flux at the interface. In this work, we use the Harten–Lax–van Leer-Discontinuities numerical flux (HLLD) with four intermediary states $\mathbf{Q}_L^\star$, $\mathbf{Q}_L^{\star\star}$, $\mathbf{Q}_R^{\star\star}$ and $\mathbf{Q}_R^\star$, divided by the waves with speeds S_L, $S_L^\star$, S_M, S_R, and $S_R^\star$, discussed in Appendix A. The states $\mathbf{Q}^\star$ and $\mathbf{Q}^{\star\star}$ are defined as

$$\mathbf{Q}_\alpha^\star = (\rho_\alpha^\star, E_\alpha^\star, \rho_\alpha^\star\mathbf{u}_\alpha^\star, \mathbf{B}_\alpha^\star, \psi_\alpha^\star) \text{ and } \mathbf{Q}_\alpha^{\star\star} = (\rho_\alpha^{\star\star}, E_\alpha^{\star\star}, \rho_\alpha^{\star\star}\mathbf{u}_\alpha^{\star\star}, \mathbf{B}_\alpha^{\star\star}, \psi_\alpha^{\star\star}),$$

with α denoting left (L) or right (R) states.

3. The same procedure is applied for B_y in the y-direction.

4. The computed values of ψ are used to update the mixed correction source term for ψ^{n+1}, computing

$$\psi^{n+1} = \exp\left(-c_h \Delta t^n \frac{c_h}{c_p^2}\right)\psi.$$

The adaptive Multiresolution (MR) method of the present paper has been designed to speed up finite volume schemes for conservation laws. In the following, a brief summary of this technique is given. For a detailed description of these strategies, we refer to [27,14,12,11,13].

The key ingredient of MR schemes are the decay properties of the wavelet coefficients of the numerical solution. The decay rate indicates the local regularity of the solution. In regions where the solution is smooth the coefficients are of small magnitude and thus coarser meshes can be used. In regions where the coefficients are significant the numerical solution is less smooth and strong gradients or even jumps are present and a fine mesh must be used [5]. Stopping the refinement in a cell at a certain scale level, where the wavelet coefficients are non-significant, leads to an adaptive MR representation.

For a finite volume scheme the uniform cell-average representation is replaced by cell-averages on an adaptive locally refined mesh, which is formed by the cells whose wavelet coefficients are significant and above a given threshold. An example of an adaptive Cartesian mesh is shown in Fig. 1. In MHD solutions localized structures are present, such as discontinuities or shocks. They could appear in different space positions in the different variables. Thus, the adaptive mesh of the MHD system is a union of the individual adaptive meshes of each quantity.

Tree structures are the natural way to store the reduced MR data. Mesh adaptivity is then related to an incomplete tree and the refinement can be interrupted at intermediate scale levels. In other words, using the tree terminology, an MR
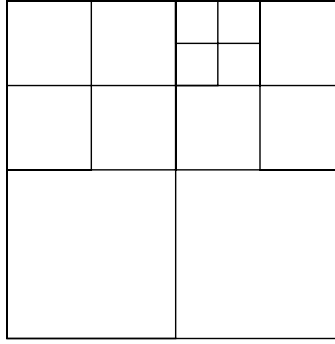
Fig. 1. Zoom in a dyadic adaptive two-dimensional Cartesian mesh. Regions where the mesh is refined are associated with detected structures in the solution, *i.e.*, where the wavelet coefficients are larger than a given threshold parameter, and therefore, they are considered as significant, and the mesh must remain refined.

mesh is formed by leaves, which are nodes without children. These leaves correspond to the cell which is being evolved in time. In summary, there are three steps in the application of an MR scheme: refinement, evolution, and coarsening. The refinement operator accounts for possible translations of the solution or the creation of finer scales in the solution between two subsequent time steps. Since the localized structures and thus the local regularity of the solution may change with time, the MR mesh at time t^n may not be sufficient any more at the next time step t^{n+1}. Hence, before evolving the solution in time, the representation of the solution should be interpolated onto an extended mesh that is expected to be a refinement of the adaptive mesh at t^n, and to contain the adaptive mesh at t^{n+1}. After that, the time evolution operator is applied to the leaves of the extended mesh. The numerical fluxes between cells of different levels are computed by adding extra cells, called virtual leaves, which will however not be used in the time evolution. Conservation is ensured by the fact that the fluxes are always computed on a higher level, the value being projected onto the leaves of a lower level. Then, wavelet thresholding is applied in order to unrefine the cells in the extended mesh (coarsening) that are not necessary for an accurate representation of the solution at t^{n+1}. This data compression is based on the definition of deletable cells, where the wavelet coefficients which are not significant, *i.e.*, their magnitudes are below the threshold parameter ϵ^ℓ, where ℓ denotes the cell scale, are called deletable cells. The data compression is given by

$$D_c = \frac{100 \sum\limits_{i=1}^{N} C_n(i)}{2^L N},$$

where N is the total number of iterations and $C_n(i)$ is the number of cells in the adaptive mesh at iteration $i \in \{1, \cdots, N\}$. The number of cells on the finest mesh is defined as 2^L, where L is the finest scale level. However, to compute the flux in a conservative form, additional neighbor cells at the same level are also necessary. These neighbor cells are not necessarily present on the adaptive mesh. Thus, if this is the case, we add these neighbor cells to the adaptive mesh, nevertheless they are not evolved in time. Therefore, the memory used is the sum of the cells of the adaptive mesh plus these neighbor cells. More details can be found in [28,27].

In order to control the L_1-norm, Harten's thresholding strategy is used, where

$$\epsilon^\ell = \frac{\epsilon^0}{|\Omega|} 2^{d(\ell-L+1)}, \ \ 0 \le \ell \le L-1, \tag{8}$$

and $d = 2$ is the space dimension and, in this two-dimensional case $|\Omega|$ is the area of the domain. Therefore, in Harten's strategy, we use a smaller value of the parameter ϵ in the coarser scales than in finer scales. For comparison, we shall also consider level independent threshold parameters: $\epsilon^\ell = \epsilon$, for all ℓ. Herein, the multiresolution analysis corresponds to a prediction operator based on third order polynomial interpolation of the cell-averages [27]. We recall that time integration is performed by a second order Runge–Kutta scheme.

5. Numerical experiments

We present here a 2D Riemann numerical experiment to illustrate the efficacy of our method compared to the traditional FV scheme. For the 2D Riemann initial condition we have used the values of the MHD variables presented in Table 1. The computational domain is $[-1, 1] \times [-1, 1]$ and Neumann boundary conditions have been applied. This example is proposed in [6], except for the boundary conditions.

We have also chosen $\gamma = 5/3$, the final time of the computations is $t = 0.1$ and $t = 0.25$, the CFL parameter $C_{CFL} = 0.3$, and $c_p^2/c_h = 0.18$. We have tested different threshold values $\epsilon^\ell = \epsilon = 0.010, 0.008$, and 0.005 and Eq. (8) with $\epsilon^0 = 0.05, 0.03,$ and 0.01.

Table 1

Initial condition of the 2D Riemann problem. The domain is $[-1, 1] \times [-1, 1]$ with Neumann boundary conditions and $\gamma = \frac{5}{3}$.

$x > 0$							
$y < 0$				$y > 0$			
ρ	ρu_x	ρu_y	ρu_z	ρ	ρu_x	ρu_y	ρu_z
1.0304	1.5774	−1.0455	−0.1016	0.9308	1.4557	−0.4633	0.0575
E	B_x	B_y	B_z	E	B_x	B_y	B_z
5.7813	0.3501	0.5078	0.1576	5.0838	0.3501	0.9830	0.3050
$x < 0$							
$y < 0$				$y > 0$			
ρ	ρu_x	ρu_y	ρu_z	ρ	ρu_x	ρu_y	ρu_z
1.0000	1.7500	−1.0000	0.0000	1.8887	0.2334	−1.7422	0.0733
E	B_x	B_y	B_z	E	B_x	B_y	B_z
6.0000	0.5642	0.5078	0.2539	12.999	0.5642	0.9830	0.4915
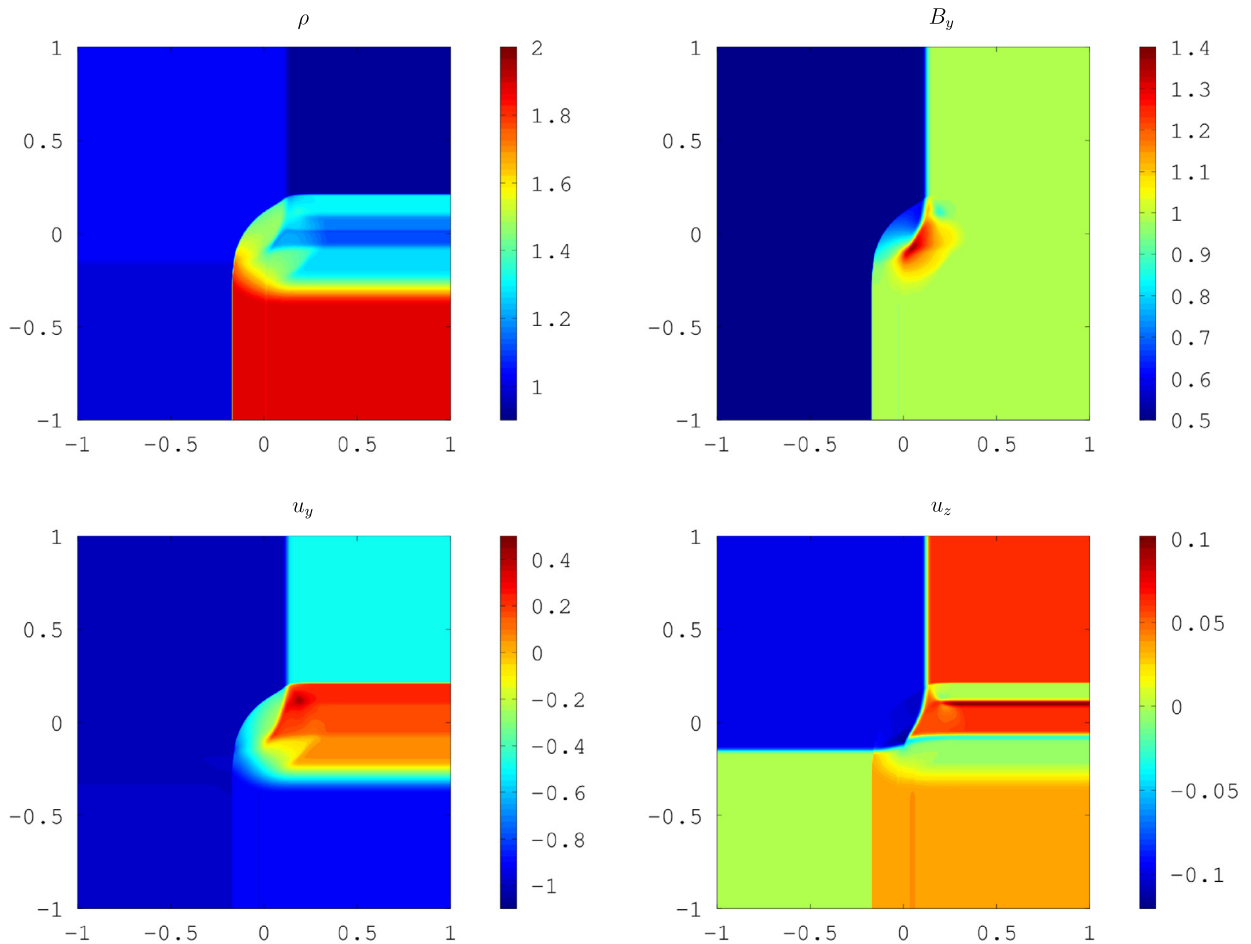
Fig. 2. FV reference solution for the 2D Riemann problem using GLM–MHD with mixed correction. Shown are variables ρ, B_y, u_y and u_z obtained at time $t = 0.1$ with $L = 11$.

The reference GLM–MHD FV code used in this work has been developed in C^{++} language, inspired by the Fortran 90 code developed by [9], including an upgrade in the routines and new features for the implementation of the numerical flux HLLD. The GLM–MHD MR code developed in [16] is based on the hydrodynamics MR Carmen code developed in [27,28]. The implementation has been optimized improving the memory allocation and unrolling the for-loops for the allocation of the variables. The CPU time is improved about a factor 4, for the test case studied here with $L = 8$ adaptive scales and $\epsilon^0 = 0.01$.

For the numerical error analysis we have used a reference solution computed with a GLM–MHD FV scheme with $L = 11$ scales using the same numerical scheme in space, implemented in the AMROC code [8], which is parallelized. We computed
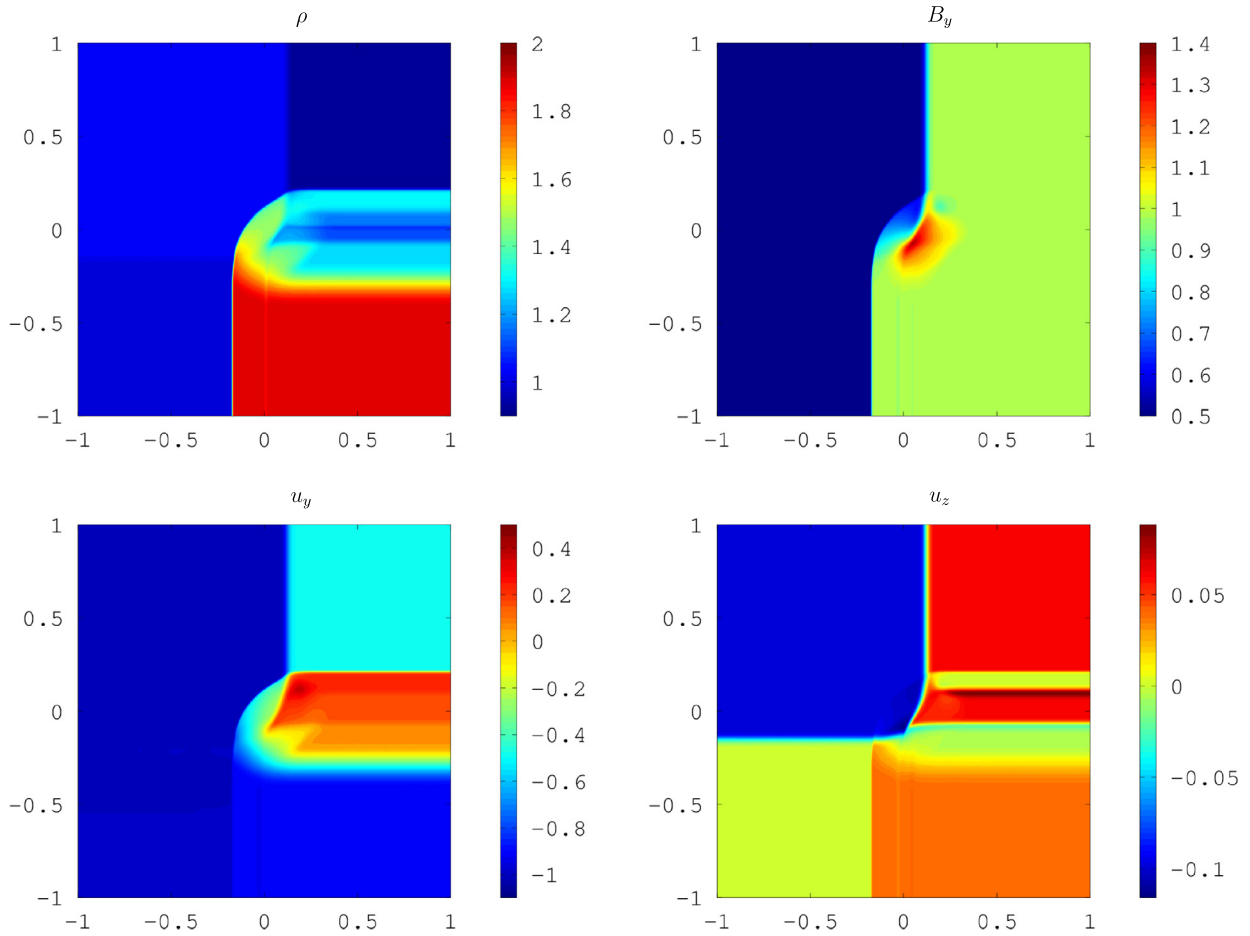
Fig. 3. MR solution with $\epsilon^0 = 0.01$ for the 2D Riemann problem using GLM–MHD with mixed correction. Shown are variables ρ, B_y, u_y and u_z obtained at time $t = 0.1$ with $L = 10$.

the L_1-error for the density solution ($L_1^e(\rho)$). The CPU time for the MHD-FV reference is obtained with another code which is not parallel.

The reference solution and numerical MR solution for $\epsilon^0 = 0.01$ and $L = 10$ at $t = 0.1$ are presented in Figs. 2 and 3, respectively. For a later time, $t = 0.25$, the numerical MR solution with $L = 9$ is presented in Fig. 7. In the solutions, we can observe that the structures are not always aligned, *e.g.*, we can identify a structure that appears in the density but not in the y-component of the magnetic field in the right part of the domain. In this region, the latter variable is almost constant. This is expected because in plasma processes the discontinuities may not necessarily occur at the same position for all quantities. The B_x component and p (not shown here) have a similar behavior as ρ, and the u_z component has a similar behavior as B_z. These observations are expected and they increase the number of cells in the adaptive mesh in the MHD case compared to the hydrodynamic case. Fig. 4 presents an example of the adaptive mesh for $\epsilon^0 = 0.01$ at the initial, intermediate and final computational time. We can observe that the adaptive meshes correspond to the structures present in the solutions.

Using the GLM–MHD method with mixed correction, the divergence of the magnetic field is not necessarily zero. However, this correction improves the convergence of the numerical solution of the MHD system to the expected physical solution, as discussed in [6]. Fig. 5 presents $|\nabla \cdot \mathbf{B}|$ for the FV reference solution for $L = 11$ and two MR solutions for $L = 10$ with $\epsilon^0 = 0.01$ at time $t = 0.1$ and $\epsilon^0 = 0.005$ at time $t = 0.25$. We observe that the maximum values of divergence are in the front transition regions, near the central part of the domain.

To check the time evolution of the divergence of the magnetic field, we consider the quantity

$$B_{\text{div}}(t) = \max\{|\nabla \cdot \mathbf{B}| : (x, y) \in [-1, 1]^2\},$$

where $\nabla \cdot \mathbf{B}$ is again evaluated using centered finite differences. Fig. 6 shows the time evolution of $B_{\text{div}}(t)$ up to $t = 0.1$ for the FV reference solution with $L = 11$ (d) and three series of MR computations with $L = 8, 9, 10$ (a, b, c) considering the following threshold, values $\epsilon = 0, 0.010, 0.008, 0.005$ and $\epsilon^0 = 0.050, 0.030, 0.010$. For the reference solution we observe a rapid decay of the initial value, around 37, during the first iterations, followed by a relaxation towards the value 3 which
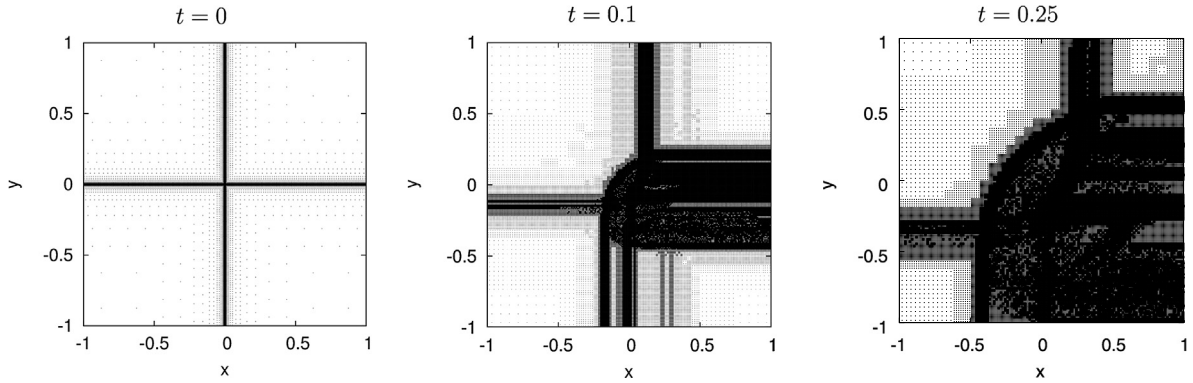
Fig. 4. Cell midpoints of the adaptive mesh with $L = 10$ of the MR computation for the 2D Riemann problem using GLM–MHD with mixed correction at time $t = 0$ with 2.30% of the cells, at $t = 0.1$ with 26.65% and $\epsilon^0 = 0.01$; and at time $t = 0.25$ with 18.37% of the cells and $\epsilon^0 = 0.05$.
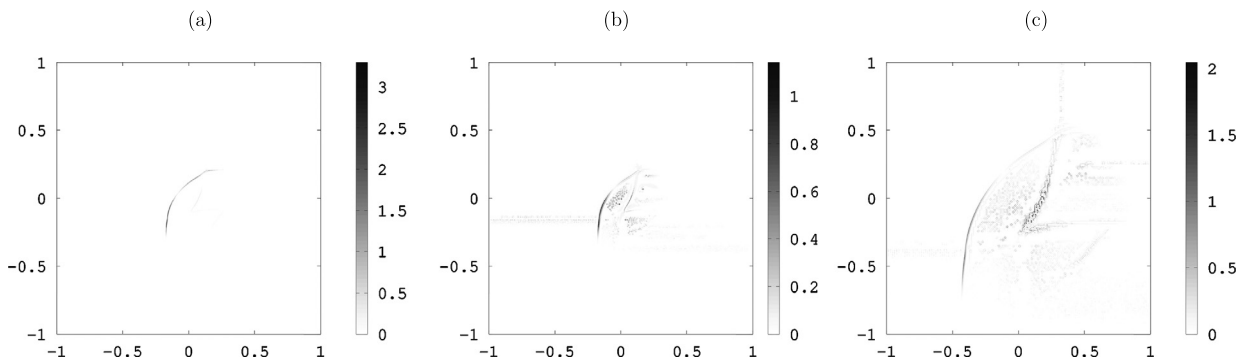
Fig. 5. Values of $|\nabla \cdot \mathbf{B}|$ for the 2D Riemann problem obtained with: (a) FV reference scheme using GLM–MHD with mixed correction for $L = 11$; (b) MR scheme with $\epsilon^0 = 0.01$ using GLM–MHD with mixed correction for $L = 10$ at time $t = 0.1$; and (c) MR scheme with $\epsilon^0 = 0.05$ using GLM–MHD with mixed correction for $L = 10$ at time $t = 0.25$. Note that the values of this quantity are mesh-dependent.

is reached at about 0.04. Afterwards, this value remains almost constant. For the MR computations we find that not only the initial but also the relaxation values of $B_{\mathrm{div}}(t)$ depend on the finest level L, and hence on the mesh size. For larger values of L the divergence becomes larger but in all cases we find that after a certain time $B_{\mathrm{div}}(t)$ becomes constant or oscillates around a mean value. Using Harten's strategy with ϵ^0 these oscillations almost disappear. In Fig. 8 we consider the evolution of $B_{\mathrm{div}}(t)$ for longer times, up to $t = 0.25$, in the MR case with $L = 9$ for $\epsilon = 0$ and 0.05, and $\epsilon^0 = 0.05$. After $t = 0.1$ no oscillations can be observed for $\epsilon = 0$, while for both $\epsilon^0 = 0.05$ and $\epsilon = 0.05$ again some oscillations appear.

One main conclusion in analyzing $B_{\mathrm{div}}(t)$ for the different cases is that no growth in time can be observed, thus the divergence error seems to be controlled by the divergence cleaning, as discussed in [20].

Considering the conservative quantities [32], we compute the energy,

$$\mathcal{E} = \int \int \left(|\mathbf{v}|^2 + |\mathbf{B}|^2 \right) dx\,dy,$$

and find the value 3.69 at the initial time. At time $t = 0.1$ we find for all FV solutions with $L = 8, 9$ and 10 the value 3.48. For the MR computations we obtain 3.46, 3.47 and 3.48 for $L = 8, 9$ and 10, respectively. These results are independent of the actual value of the threshold (ranging from 0.01 down to 0) and there is no significant influence if a fixed or level dependent value is used. This means that in all computations about 94% of the energy is conserved. At later time, $t = 0.25$, we observe some decay, but still about 86% of the energy is conserved.

The total magnetic helicity is also a conservative quantity of the ideal MHD equations [3] and we consider its time rate of change, defined as,

$$\frac{\partial H}{\partial t} = 2 \int \int \mathbf{B} \cdot (\mathbf{u} \times \mathbf{B}) \, dx\,dy.$$

As shown in Fig. 8, right, the reference solution conserves perfectly the total magnetic helicity and $\partial H / \partial t$ yields values close to machine precision. For the three MR solutions there is an initial peak at about $4 \cdot 10^{-12}$ which immediately decays
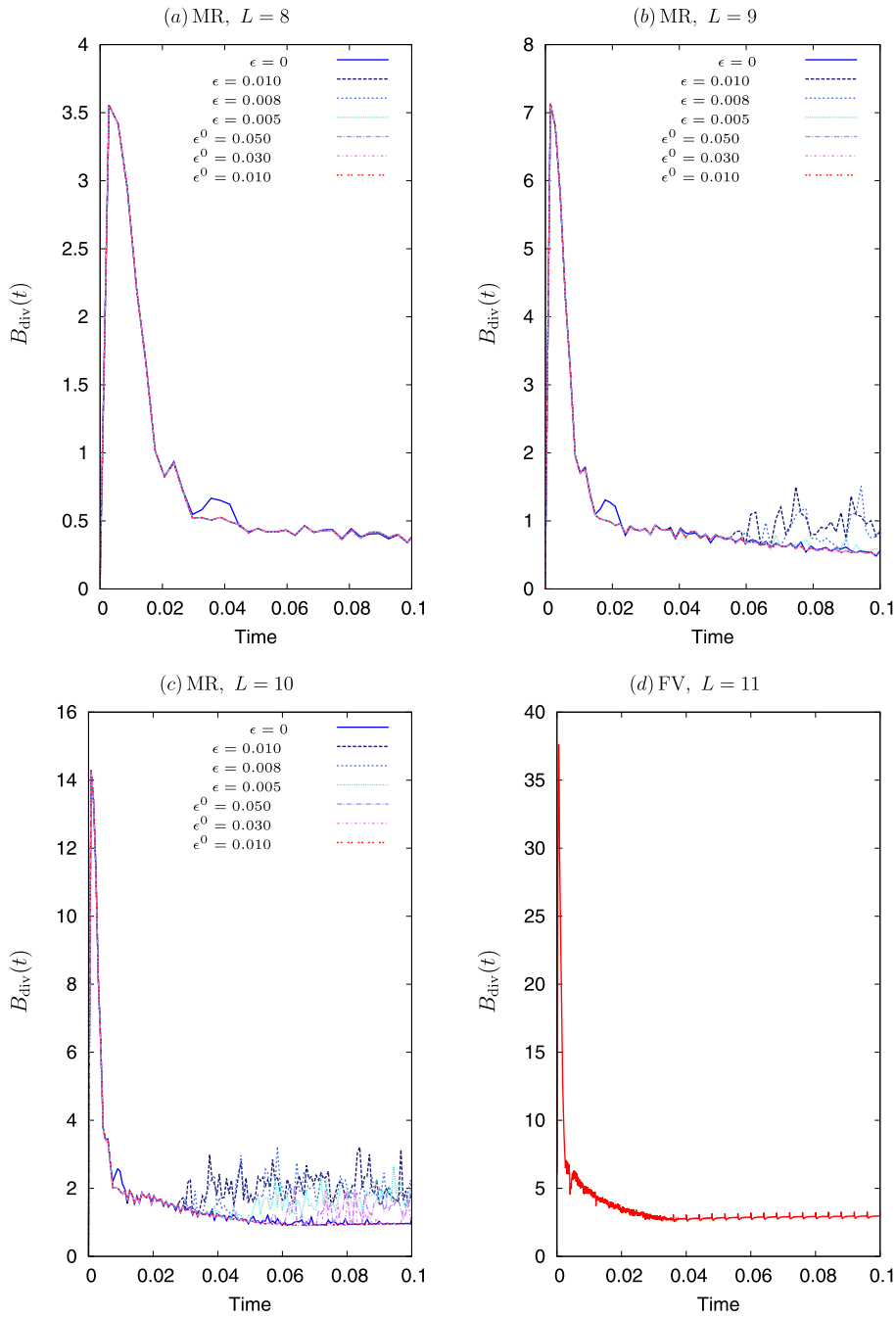
Fig. 6. The quantity $B_{\text{div}}(t)$ over time for the 2D Riemann problem, with: (a, b, c) GLM–MHD with mixed correction using the MR scheme with $\epsilon^\ell = \epsilon = 0.010, 0.008, 0.005$ and $\epsilon^0 = 0, 0.05, 0.03, 0.01$ for $L = 8, 9, 10$; (d) GLM–MHD with mixed correction using the FV scheme for the reference solution with $L = 11$.

to near zero machine precision, and remains zero for $\epsilon = 0$. For the two others threshold values some intermittent spikes with amplitude below $2 \cdot 10^{-13}$ are observed.

Table 2 presents a summary of the CPU time, memory compression, D_c and $L_1^e(\rho)$ for all experiments at time $t = 0.1$. For $\epsilon^\ell = \epsilon = 0.005$ and $\epsilon^0 = 0.05$ the results are close, independent of the maximum level L. However, the case $\epsilon = 0.005$ has slightly better CPU time and memory compression with respect to $L_1^e(\rho)$. In these cases, for $L = 10$, the CPU time is about 7–14% of the FV CPU time and the errors are approximately of order 10^{-2}. As expected, the error increases for a scale-independent threshold $\epsilon^\ell = \epsilon$ with ϵ being large, because it does not control well the error. However, as we decrease the value of ϵ, the error becomes smaller. Thus, the choice of ϵ is an important ingredient. We can observe that if we
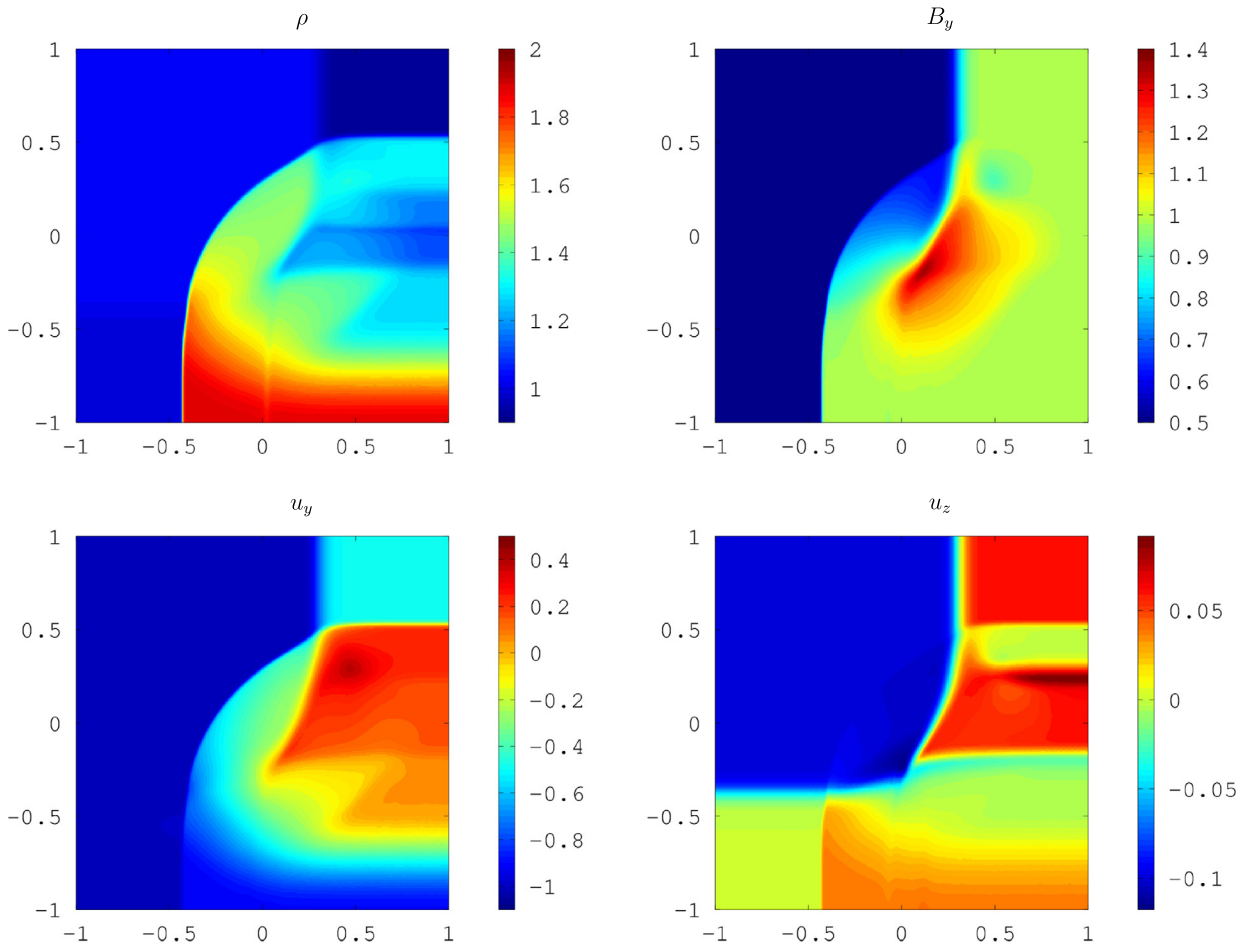
Fig. 7. MR solution for the 2D Riemann problem using GLM–MHD with mixed correction for $\epsilon^0 = 0.05$. Shown are variables ρ, B_y, u_y and u_z obtained at time $t = 0.25$ with $L = 9$.

choose a sufficiently small ϵ, both strategies have similar behavior. However, we can optimize this process by using Harten's strategy, which corresponds to a level dependent ϵ.

In Table 3 we show the CPU time, memory compression, D_c, and $L_1^e(\rho)$ results for all experiments done at time $t = 0.25$. We present the simulations for $\epsilon^\ell = \epsilon = 0.005$ and $\epsilon^0 = 0.05$. The results at $t = 0.25$ show that the MR approach does not introduce growing instabilities and it is possible to compute the solution for larger values of t.

6. Conclusions and perspectives

Starting from the ideal MHD equations completed with generalized Lagrangian multipliers to control the incompressibility of the magnetic field, we have developed an adaptive multiresolution method in two space dimensions on a Cartesian mesh with local mesh refinement. The space discretization is based on finite volumes with an HLLD numerical flux. For time integration an explicit Runge–Kutta scheme has been applied. To introduce a locally refined spatial mesh and also for local interpolation of the flux values Harten's cell average multiresolution analysis has been used.

To assess the efficiency and quality of this new adaptive scheme, we have considered a two-dimensional Riemann problem. We compared this numerical solution with adaptive MR results for different threshold values and two strategies of varying resolution levels. The numerical results show that the divergence cleaning can indeed work successfully with adaptive space discretizations. The MR method with constant threshold exhibits better CPU time performance but worse precision when compared to the level dependent threshold. The only drawback with respect to the level dependent threshold computations is that the number of cells on the adaptive mesh is increased. We also observed that energy and the time rate of change of magnetic helicity, both conserved quantities in the ideal MHD equations, remain indeed approximately conserved in our adaptive MR computations.
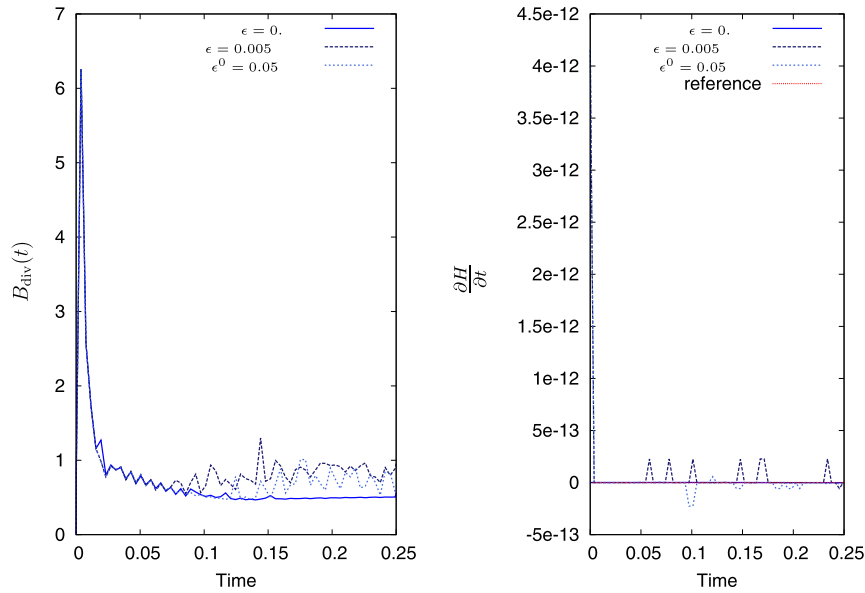
Fig. 8. The quantity $B_{\mathrm{div}}(t)$ and the time rate of change of magnetic helicity over time for the 2D Riemann problem, obtained with GLM–MHD with the mixed correction MR scheme using $\epsilon^\ell = \epsilon = 0, 0.005$ and $\epsilon^0 = 0.05$ for $L = 9$ and for the reference solution.

Table 2
CPU time, memory, D_c, and density error $L_1^e(\rho)$ for the 2D Riemann problem computed with the MR scheme using GLM–MHD with mixed correction and either with constant or level dependent threshold for $t = 0.1$.

$L = 8$	MR						FV
	$\epsilon^\ell = \epsilon$			ϵ^0			
	0.01	0.008	0.005	0.05	0.03	0.01	
CPU time (%)	22.74	23.47	24.55	26.71	27.80	30.33	100
Memory (%)	44.18	45.38	47.70	51.03	53.12	56.47	100
D_c (%)	29.74	30.67	32.50	34.94	36.60	39.28	100
$L_1^e(\rho) \cdot 10^{-2}$	3.680	3.669	3.657	3.657	3.652	3.651	3.640
$L = 9$	MR						FV
	$\epsilon^\ell = \epsilon$			ϵ^0			
	0.01	0.008	0.005	0.05	0.03	0.01	
CPU time (%)	13.63	14.66	15.91	17.67	19.00	20.46	100
Memory (%)	27.03	28.79	31.24	34.34	36.01	39.20	100
D_c (%)	17.70	18.97	21.01	23.51	24.92	27.42	100
$L_1^e(\rho) \cdot 10^{-2}$	2.086	2.039	1.981	1.974	1.958	1.953	1.9409
$L = 10$	MR						FV
	$\epsilon^\ell = \epsilon$			ϵ^0			
	0.01	0.008	0.005	0.05	0.03	0.01	
CPU time (%)	7.73	8.71	9.85	12.00	13.03	14.67	100
Memory	14.66	16.02	18.82	22.40	24.46	27.48	100
D_c (%)	9.25	10.07	12.01	14.66	16.49	19.25	100
$L_1^e(\rho) \cdot 10^{-2}$	1.090	1.031	0.932	0.905	0.875	0.851	0.841

NOTE: The results are computed with second-order Runge–Kutta for the MR scheme. The CPU time for the GLM–MHD FV method is 277 sec., 2326 sec. and 314 min., for $L = 8, 9$ and 10, for an Intel(R) Xeon(R) CPU E5620 @ 2.40 GHz, CPU 1596 MHz, cache size 12 288 KB and 4 cores. CPU time, memory, and D_c performances are computed with the corresponding non-adaptive FV solution using $L = 8, 9$ and 10 scales on a uniform level. For the error, in all cases, we use a reference solution computed with a GLM–MHD FV scheme with $L = 11$ for the same numerical scheme implemented in the AMROC code [8].

In future work, we plan to complete the adaptive method with time adaptivity using local and controlled time stepping and to perform thus fully adaptive simulations in three space dimensions. A second interesting direction is to move to non-ideal MHD, taking into account resistive effects and finite values of the fluid viscosity to study the physics of reconnection of current sheets, especially in space physics applications.

Table 3
CPU time, memory, D_c, and density error $L_1^e(\rho)$ for the 2D Riemann problem simulated with the MR scheme using GLM–MHD with mixed correction and with constant or level dependent threshold for $t = 0.25$.

$L = 9$	MR		FV
	$\epsilon^\ell = 0.005$	$\epsilon^0 = 0.05$	
CPU time (%)	18.79	22.61	100
Memory (%)	38.12	45.25	100
D_c (%)	23.80	29.03	100
$L_1^e(\rho) \cdot 10^{-2}$	3.887	3.826	3.694

Acknowledgements

Appendix A. HLLD Riemann solver

In the following solver, we consider the one-dimensional GLM–MHD equations in their primitive form

$$\frac{\partial \rho}{\partial t} + \frac{\partial \rho u_x}{\partial x} = 0, \tag{9a}$$

$$\frac{\partial E}{\partial t} + \frac{\partial}{\partial x}\left[\left(E + p + \frac{\mathbf{B}^2}{2}\right)u_x - \left(u_x B_x + u_y B_y + u_z B_z\right)B_x\right] = 0, \tag{9b}$$

$$\frac{\partial (\rho u_x)}{\partial t} + \frac{\partial}{\partial x}\left[\rho u_x^2 + p + \left(\frac{\mathbf{B}^2}{2}\right) - B_x^2\right] = 0, \tag{9c}$$

$$\frac{\partial (\rho u_y)}{\partial t} + \frac{\partial}{\partial x}\left(\rho u_x u_y - B_x B_y\right) = 0, \tag{9d}$$

$$\frac{\partial (\rho u_z)}{\partial t} + \frac{\partial}{\partial x}\left(\rho u_x u_z - B_x B_z\right) = 0, \tag{9e}$$

$$\frac{\partial B_x}{\partial t} + \frac{\partial \psi}{\partial x} = 0, \tag{9f}$$

$$\frac{\partial B_y}{\partial t} + \frac{\partial}{\partial x}\left(u_x B_y - B_x u_y\right) = 0, \tag{9g}$$

$$\frac{\partial B_z}{\partial t} + \frac{\partial}{\partial x}\left(u_x B_z - B_x u_z\right) = 0, \tag{9h}$$

$$\frac{\partial \psi}{\partial t} + c_h^2 \frac{\partial B_x}{\partial x} = -\frac{c_h^2}{c_p^2}\psi. \tag{9i}$$

Considering the above system we can obtain the Jacobian matrix. From the structure of this matrix one can verify that the equations of B_x and ψ can be decoupled from the remaining system and we can obtain the Jacobian matrix for the 1D MHD system [6, pp. 651–653]. The eigenvalues of this matrix are u_x, $u_x \pm c_s$, $u_x \pm c_a$ and $u_x \pm c_f$, where c_s, c_f are the slow and fast magneto-acoustic waves and c_a is the Alfvén wave.

The Harten–Lax–van Leer-Discontinuities (HLLD) solver for MHD was firstly developed by Miyoshi and Kusano [22] and it can be considered as an extension of the Harten–Lax–van Leer (HLL) solver presented in [19]. The HLLD solver is based on four intermediary states $\mathbf{Q}_L^\star$, $\mathbf{Q}_L^{\star\star}$, $\mathbf{Q}_R^{\star\star}$ and $\mathbf{Q}_R^\star$, divided by five waves S_L, $S_L^\star$, S_M, $S_R^\star$ and S_R, as illustrated in Fig. 9. These waves are related to entropy, fast and Alfvén waves. The HLLD numerical flux can resolve isolated discontinuities in the solution of the MHD system. This solver preserves positivity and is more robust and efficient than the linearized solver, with an equally good resolution.

The states $\mathbf{Q}^\star$ and $\mathbf{Q}^{\star\star}$ for the GLM–MHD system are defined as

$$\mathbf{Q}_\alpha^\star = (\rho_\alpha^\star, E_\alpha^\star, \rho_\alpha^\star \mathbf{u}_\alpha^\star, \mathbf{B}_\alpha^\star, \psi_\alpha^\star) \quad \text{and} \quad \mathbf{Q}_\alpha^{\star\star} = (\rho_\alpha^{\star\star}, E_\alpha^{\star\star}, \rho_\alpha^{\star\star}\mathbf{u}_\alpha^{\star\star}, \mathbf{B}_\alpha^{\star\star}, \psi_\alpha^{\star\star}),$$
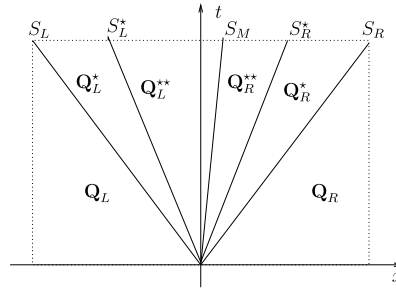
Fig. 9. Schematic of the Riemann fan structure with four intermediate states used in the HLLD flux. Adapted from [22].

with α denoting left (L) or right (R) states. In this approach, we compute the numerical flux for ψ directly. Then we consider $\psi^\star = \psi^{\star\star} = \psi$ here in the intermediary vector states, recalling that the HLLD is originally designed for the MHD system, where the vector state $\mathbf{Q}$ does not include the variable ψ.

The numerical flux function is given by

$$
\mathbf{F}_{HLLD} = \begin{cases}
\mathbf{F}_L, & \text{if } S_L > 0, \\
\mathbf{F}_L^\star, & \text{if } S_L \leq 0 \leq S_L^\star, \\
\mathbf{F}_L^{\star\star}, & \text{if } S_L^\star \leq 0 \leq S_M, \\
\mathbf{F}_R^{\star\star}, & \text{if } S_M \leq 0 \leq S_R^\star, \\
\mathbf{F}_R^\star, & \text{if } S_R^\star \leq 0 \leq S_R, \\
\mathbf{F}_R, & \text{if } S_R < 0.
\end{cases}
\tag{10}
$$

The flux vectors $\mathbf{F}_L = \mathbf{F}(\mathbf{Q}_L)$, $\mathbf{F}_R = \mathbf{F}(\mathbf{Q}_R)$ are exact, while $\mathbf{F}_L^\star$, $\mathbf{F}_R^\star$ are approximate fluxes at intermediary states $\mathbf{Q}_L^\star$, $\mathbf{Q}_R^\star$, and $\mathbf{F}_L^{\star\star}$, $\mathbf{F}_R^{\star\star}$ are approximate fluxes at intermediary states $\mathbf{Q}_L^{\star\star}$, $\mathbf{Q}_R^{\star\star}$.

By the following process, we present the variables of the states $\mathbf{Q}_\alpha^\star$ and $\mathbf{Q}_\alpha^{\star\star}$, allowing us to compute the HLLD flux in the intermediary states

$$
\mathbf{F}_\alpha^\star = \mathbf{F}_\alpha + S_\alpha (\mathbf{Q}_\alpha^\star - \mathbf{Q}_\alpha),
$$
$$
\mathbf{F}_\alpha^{\star\star} = \mathbf{F}_\alpha + S_\alpha^\star \mathbf{Q}_\alpha^{\star\star} - (S_\alpha^\star - S_\alpha) \mathbf{Q}_\alpha^\star - S_\alpha \mathbf{Q}_\alpha,
\tag{11}
$$

where $\alpha = R$ and L denote right and left, respectively.

The following description of the HLLD flux is related to the x-direction, considering $B_x^\star = B_x^{\star\star} = B_x$. In two-dimensions, a similar expression can be obtained in the y-direction, considering $B_y^\star = B_y^{\star\star} = B_y$.

There are different possibilities to approximate the propagation speeds S_α; for instance, we use

$$
S_L = \min(u_L, u_R) - \max(c_{f_L}, c_{f_R}), \quad S_R = \max(u_L, u_R) + \max(c_{f_L}, c_{f_R}),
\tag{12}
$$

where u_α are the plasma velocities, c_{f_α} are the magnetic acoustic waves [25]. The choice of S_M is made to estimate the average normal velocity and it is given by

$$
S_M = \frac{(S_R - u_{x_R})\rho_R \, u_{x_R} - (S_L - u_{x_L})\rho_L \, u_{x_L} - p_{T_R} + p_{T_L}}{(S_R - u_{x_R})\rho_R - (S_L - u_{x_L})\rho_L}.
\tag{13}
$$

The velocity is assumed to be constant over the Riemann fan, *i.e.*,

$$
u_{x_L}^\star = u_{x_L}^{\star\star} = u_{x_R}^{\star\star} = u_{x_R}^\star = S_M.
\tag{14}
$$

The total pressure $p_T = p + \frac{\mathbf{B} \cdot \mathbf{B}}{2}$ is also kept constant,

$$
p_{T_L}^\star = p_{T_L}^{\star\star} = p_{T_R}^{\star\star} = p_{T_R}^\star = p_T^\star.
\tag{15}
$$

Under these conditions tangential and rotational discontinuities can be formed in the Riemann fan.

From the choice of S_M, the pressure $p_T^\star$ can be written as

$$
p_T^\star = \frac{(S_R - u_{x_R})\rho_R \, p_{T_L} - (S_L - u_{x_L})\rho_L \, p_{T_R}}{(S_R - u_{x_R})\rho_R - (S_L - u_{x_L})\rho_L} + \frac{\rho_L \, \rho_R (S_R - u_{x_R})(S_L - u_{x_L})(u_{x_R} - u_{x_L})}{(S_R - u_{x_R})\rho_R - (S_L - u_{x_L})\rho_L}.
\tag{16}
$$

Given S_M and $p_T^\star$, the states $\mathbf{Q}_\alpha^\star = (\rho_\alpha^\star, p_\alpha^\star, u_{x_\alpha}^\star, u_{y_\alpha}^\star, u_{z_\alpha}^\star, B_{x_\alpha}^\star, B_{y_\alpha}^\star, B_{z_\alpha}^\star)$ are bordered by the states $\mathbf{Q}_\alpha$ and they can be obtained from the jumps along S_α, where $\alpha = L$ or R represents the left or right state. Therefore, one can derive the variables of the states $\mathbf{Q}_\alpha^\star$ as

$$\rho_\alpha^\star = \rho_\alpha \frac{S_\alpha - u_{x_\alpha}}{S_\alpha - S_M}, \tag{17a}$$

$$u_{y_\alpha}^\star = u_{y_\alpha} - B_x B_{y_\alpha} \frac{S_M - u_{x_\alpha}}{\rho_\alpha(S_\alpha - u_{x_\alpha})(S_\alpha - S_M) - B_x^2}, \tag{17b}$$

$$u_{z_\alpha}^\star = u_{z_\alpha} - B_x B_{z_\alpha} \frac{S_M - u_{x_\alpha}}{\rho_\alpha(S_\alpha - u_{x_\alpha})(S_\alpha - S_M) - B_x^2}, \tag{17c}$$

$$B_{y_\alpha}^\star = B_{y_\alpha} \frac{\rho_\alpha(S_\alpha - u_{x_\alpha})^2 - B_x^2}{\rho_\alpha(S_\alpha - u_{x_\alpha})(S_\alpha - S_M) - B_x^2}, \tag{17d}$$

$$B_{z_\alpha}^\star = B_{z_\alpha} \frac{\rho_\alpha(S_\alpha - u_{x_\alpha})^2 - B_x^2}{\rho_\alpha(S_\alpha - u_{x_\alpha})(S_\alpha - S_M) - B_x^2}. \tag{17e}$$

Consequently, we can compute $E_\alpha^\star$

$$E_\alpha^\star = \frac{(S_\alpha - u_{x_\alpha})E_\alpha - p_{T_\alpha}u_{x_\alpha} + p_T^\star S_M + B_x(\mathbf{u}_\alpha \cdot \mathbf{B}_\alpha - \mathbf{u}_\alpha^\star \cdot \mathbf{B}_\alpha^\star)}{S_\alpha - S_M}. \tag{18}$$

During the computations some divisions by zero of the type 0/0 can appear when $S_M = u_{x_\alpha}$, $S_\alpha = u_{x_\alpha} \pm c_{f_\alpha}$, $B_{y_\alpha} = B_{z_\alpha} = 0$ and $B_x^2 \geq \gamma\, p_\alpha$. In these cases, we have to replace $u_{y_\alpha}^\star = u_{y_\alpha}$, $u_{z_\alpha}^\star = u_{z_\alpha}$, and $B_{y_\alpha}^\star = B_{z_\alpha}^\star = 0$.

Similarly, it is possible to obtain the equations related to the states

$$\mathbf{Q}_\alpha^{\star\star} = (\rho_\alpha^{\star\star}, p_\alpha^{\star\star}, u_{x_\alpha}^{\star\star}, u_{y_\alpha}^{\star\star}, u_{z_\alpha}^{\star\star}, B_{x_\alpha}^{\star\star}, B_{y_\alpha}^{\star\star}, B_{z_\alpha}^{\star\star}).$$

Due to the relation described by Eq. (14), starting with the jump condition of the continuity equation over an arbitrary value S, where $S_L < S < S_M$ or $S_M < S < S_R$, we have

$$\rho_\alpha^{\star\star} = \rho_\alpha^\star. \tag{19}$$

The propagation velocities of the Alfvén waves in the intermediary states are estimated by

$$S_L^\star = S_M - \frac{|B_x|}{\sqrt{\rho_L^\star}}, \qquad S_R^\star = S_M - \frac{|B_x|}{\sqrt{\rho_R^\star}}. \tag{20}$$

Considering the jump conditions to the tangential components of the velocity and magnetic field over S_M, and if $B_x \neq 0$, we can obtain the following relations

$$u_{y_L}^{\star\star} = u_{y_R}^{\star\star} \equiv u_y^{\star\star}, \quad u_{z_L}^{\star\star} = u_{z_R}^{\star\star} \equiv u_z^{\star\star}, \tag{21a}$$

$$B_{y_L}^{\star\star} = B_{y_R}^{\star\star} \equiv B_y^{\star\star}, \quad B_{z_L}^{\star\star} = B_{z_R}^{\star\star} \equiv B_z^{\star\star}. \tag{21b}$$

If $B_x = 0$, it is impossible to calculate the remaining variables of the states $\mathbf{Q}_\alpha^{\star\star}$. Replacing Eqs. (19)–(21) into the integral conservation laws over the Riemann fan, we can derive the variables

$$u_y^{\star\star} = \frac{u_{y_L}^\star + \sqrt{\rho_R^\star}u_{y_R}^\star + (B_{y_R}^\star - B_{y_L}^\star)\text{sign}(B_x)}{\sqrt{\rho_L^\star} + \sqrt{\rho_R^\star}}, \tag{22a}$$

$$u_z^{\star\star} = \frac{\sqrt{\rho_L^\star}u_{z_L}^\star + \sqrt{\rho_R^\star}u_{z_R}^\star + (B_{z_R}^\star - B_{z_L}^\star)\text{sign}(B_x)}{\sqrt{\rho_L^\star} + \sqrt{\rho_R^\star}}, \tag{22b}$$

$$B_y^{\star\star} = \frac{\sqrt{\rho_L^\star}B_{y_R}^\star + \sqrt{\rho_R^\star}B_{y_L}^\star + \sqrt{\rho_L^\star \rho_R^\star}(u_{y_R}^\star - u_{y_L}^\star)\text{sign}(B_x)}{\sqrt{\rho_L^\star} + \sqrt{\rho_R^\star}}, \tag{22c}$$

$$B_z^{\star\star} = \frac{\sqrt{\rho_L^\star}B_{z_R}^\star + \sqrt{\rho_R^\star}B_{z_L}^\star + \sqrt{\rho_L^\star \rho_R^\star}(u_{z_R}^\star - u_{z_L}^\star)\text{sign}(B_x)}{\sqrt{\rho_L^\star} + \sqrt{\rho_R^\star}}, \tag{22d}$$

where $\text{sign}(B_x)$ is 1 for $B_x > 0$, and -1 for $B_x < 0$. Consequently, the equation of the energy in $\mathbf{Q}^{\star\star}$ is given by

$$E_\alpha^{\star\star} = E_\alpha^\star \mp \sqrt{\rho_\alpha^\star}\left(\mathbf{u}_\alpha^\star \cdot \mathbf{B}_\alpha^\star - \mathbf{u}_\alpha^{\star\star} \cdot \mathbf{B}_\alpha^{\star\star}\right)\text{sign}(B_x). \tag{23}$$

The same procedure is applied for the y-direction.

References

[1] F. Assous, P. Degond, E. Heintze, P.A. Raviart, J. Segre, On a finite-element method for solving the three-dimensional Maxwell equations, J. Comput. Phys. 109 (2) (1993) 222–237.

[2] D.S. Balsara, Divergence-free reconstruction of magnetic fields and WENO schemes for magnetohydrodynamics, J. Comput. Phys. 228 (2009) 5040–5056.

[3] P.M. Bellan, Fundamentals of Plasma Physics, Cambridge University Press, 2006.

[4] J.U. Brackbill, D.C. Barnes, Note: the effect of nonzero $\nabla \cdot \mathbf{B}$ on the numerical solution of the magnetohydrodynamic equations, J. Comput. Phys. 35 (3) (1980) 426–430.

[5] A. Cohen, S.M. Kaber, S. Müller, M. Postel, Fully adaptive multiresolution finite volume schemes for conservation laws, Math. Comput. 72 (241) (2003) 183–225.

[6] A. Dedner, F. Kemm, D. Kröner, C.-D. Munz, T. Schnitzer, M. Wesenberg, Hyperbolic divergence cleaning for the MHD equations, J. Comput. Phys. 175 (2002) 645–673.

[7] A. Dedner, C. Rohde, M. Wesenberg, A new approach to divergence cleaning in magnetohydrodynamic simulations, in: T.Y. Hou, T. Eitan (Eds.), Hyperbolic Problems: Theory, Numerics, Applications, Springer, Berlin, 2003, pp. 509–518.

[8] R. Deiterding, M.O. Domingues, S.M. Gomes, O. Roussel, K. Schneider, Adaptive multiresolution or adaptive mesh refinement: a case study for 2D Euler equations, ESAIM Proc. 29 (2009) 28–42.

[9] B. Di Pierro, Méthode d'annulation de la divergence pour les EDP hyperboliques application aux équations de la magnéto-hydrodynamique, Project Master Course, Université de Provence, Marseille, France, 2009 (unpublished, in French).

[10] M.O. Domingues, A.K.F. Gomes, S.M. Gomes, O. Mendes, B. Di Pierro, K. Schneider, Extended generalized Lagrangian multipliers for magnetohydrodynamics using adaptive multiresolution methods, ESAIM Proc. 43 (December 2013) 95–107.

[11] M.O. Domingues, S.M. Gomes, O. Roussel, K. Schneider, An adaptive multiresolution scheme with local time stepping for evolutionary PDEs, J. Comput. Phys. 227 (8) (2008) 3758–3780.

[12] M.O. Domingues, S.M. Gomes, O. Roussel, K. Schneider, Space–time adaptive multiresolution methods for hyperbolic conservation laws: applications to compressible Euler equations, Appl. Numer. Math. 59 (2009) 2303–2311.

[13] M.O. Domingues, S.M. Gomes, O. Roussel, K. Schneider, Adaptive multiresolution methods, ESAIM Proc. 34 (2011) 1–96.

[14] M.O. Domingues, O. Roussel, K. Schneider, An adaptive multiresolution method for parabolic PDEs with time-step control, Int. J. Numer. Methods Eng. 78 (2009) 652–670.

[15] J.P. Freidberg, Ideal MHD, Cambridge University Press, 2014.

[16] A.K.F. Gomes, Análise multirresolução adaptativa no contexto da resolução numérica de um modelo de magnetohidrodinâmica ideal, Master's thesis, Instituto Nacional de Pesquisas Espaciais (INPE), São José dos Campos, 2012-09-13, http://urlib.net/8JMKD3MGP7W/3CE6FSE.

[17] A. Harten, Multiresolution algorithms for the numerical solution of hyperbolic conservation laws, Commun. Pure Appl. Math. 48 (1995) 1305–1342.

[18] A. Harten, Multiresolution representation of data: a general framework, SIAM J. Numer. Anal. 33 (3) (1996) 385–394.

[19] A. Harten, P.D. Lax, B. van Leer, On upstream differencing and Godunov-type schemes for hyperbolic conservation laws, SIAM Rev. 25 (1983) 35.

[20] S.S. Komissarov, M. Barkov, M. Lyutikov, Tearing instability in relativistic magnetically dominated plasmas, Mon. Not. R. Astron. Soc. 374 (2007) 415–426.

[21] A. Mignone, P. Tzeferacos, A second-order unsplit Godunov scheme for cell-centered MHD: the CTU–GLM scheme, J. Comput. Phys. 229 (6) (2010) 2117–2138.

[22] T. Miyoshi, K. Kusano, A multi-state HLL approximate Riemann solver for ideal magnetohydrodynamics, J. Comput. Phys. 208 (2005) 315–344.

[23] S. Müller, Adaptive Multiscale Schemes for Conservation Laws, Lectures Notes in Computational Science and Engineering, vol. 27, Springer, Heidelberg, 2003.

[24] C.-D. Munz, P. Ommes, R. Schneider, E. Sonnendrücker, U. Voss, Divergence corrections techniques for Maxwell solvers based on a hyperbolic model, J. Comput. Phys. 161 (2) (2000) 484.

[25] K.G. Powell, An approximate Riemann solver for magnetohydrodynamics (that works in more than one dimension), Technical report 1, NASA Langley Research Center, Hampton, 1994.

[26] K.G. Powell, P.L. Roe, T.J. Linde, T.I. Gombosi, D.L. De Zeeuw, A solution-adaptive upwind scheme for ideal magnetohydrodynamics, J. Comput. Phys. 154 (1999) 284–309.

[27] O. Rousell, K. Schneider, A. Tsigulin, H. Bockhorn, A conservative fully adaptative multiresolution algorithm for parabolic PDEs, J. Comput. Phys. 188 (2003) 493–523.

[28] O. Roussel, Development of a 3D adaptive multiresolution algorithm for the resolution of parabolic PDEs. Application to thermo-diffusive flame instabilities, PhD thesis, Université de la Méditerranée, Marseille, 2003.

[29] G. Tóth, The $\nabla \cdot \mathbf{B}$ constraint in shock-capturing magnetohydrodynamics codes, J. Comput. Phys. 161 (2000) 605–652.

[30] G. Tóth, B. van der Holst, I.V. Sokolov, D.L. De Zeeuw, T.I. Gombosi, F. Fang, W.B. Manchester, X. Meng, D. Najib, K.G. Powell, Q.F. Stout, A. Glocer, Y.-J. Ma, M. Opher, Adaptive numerical algorithms in space weather modeling, J. Comput. Phys. 231 (3) (2012) 870–903.

[31] T.S. Tricco, D.J. Price, Constrained hyperbolic divergence cleaning for smoothed particle magnetohydrodynamics, J. Comput. Phys. 231 (21) (2012) 7214–7236.

[32] Y. Xinwei, A note on the energy conservation of the ideal MHD equations, Nonlinearity 22 (4) (2009) 913.